Identifying Cu(II)–amyloid peptide binding intermediates in the early stages of aggregation by resonance Raman spectroscopy: a simulation study†

Hao Ren, [a] Yu Zhang,‡*[b] Sibei Guo,[c] Na Lin, [d] Li Deng,[a] Tongtao Yue [a] and Fang Huang*[a]

The aggregation of amyloid beta (Aβ) peptides plays a crucial role in the pathology and etiology of Alzheimer's disease. Experimental evidence shows that copper ion is an aggregation-prone species with the ability to coordinately bind to Aβ and further induce the formation of neurotoxic Aβ oligomers. However, the detailed structures of Cu(II)–Aβ complexes have not been illustrated, and the kinetics and dynamics of the Cu(II) binding are not well understood. Two Cu(II)–Aβ complexes have been proposed to exist under physiological conditions, and another two might exist at higher pH values. By using *ab initio* simulations for the spontaneous resonance Raman and time domain stimulated resonance Raman spectroscopy signals, we obtained the characteristic Raman vibronic features of each complex. These signals contain rich structural information with high temporal resolution, enabling the characterization of transient states during the fast Cu–Aβ binding and interconversion processes.

I. Introduction

Alzheimer's disease (AD), a progressive irreversible neurological disorder, is the most common cause of dementia.[1–4] AD attacks our society and brings an immense amount of economic and mental loss. Although the pathology and etiology of AD are not yet well understood, it is believed that the aggregation of amyloid β (Aβ) peptides plays a crucial role in the development of this disease.[4–6] Aβ peptides are the major constituents of senile plaques, which are a hallmark of AD. Previous studies have shown that Aβ oligomers are the most neurotoxic due to their interaction with cell membranes and their roles in the production of reactive oxygen species (ROS).[7,8] Specifically, transition metal ions, such as Cu^{2+} and Zn^{2+}, exhibit abnormally high concentrations in the senile plaque, the brain and the synaptic cleft.[5,9–14] Various experiments have provided evidence that these metal ions are involved in the aggregation of Aβ. For example, copper ions were proposed to promote Aβ aggregation and to play important roles in the AD cascade.[4,12,15,16]

The binding between Aβ and Cu(II) has been studied extensively, and it is well established that two equatorial coordination modes coexist under physiological conditions.[3,15–17] It was shown that Cu(II) binds to Aβ and forms complex I [Fig. 1 (a)] at a diffusion-limited rate in milliseconds. It can be converted to complex II [Fig. 1(b)] at a lower rate. The latter is relatively inert and has been viewed as a reservoir for Aβ monomers that can only aggregate through reversed conversion to complex I.[15] Under physiological conditions, complex I dominates in lower pH environments and complex II dominates as the pH increases above 7.8. *In vitro* experiments showed that the other two complexes, III and IV [Fig. 1(c) and (d)], appear as the pH is further increased above 9.3 and 10.2, respectively.[17] Details about the structural, kinetic, and dynamical features of these complexes will facilitate the uncovering of the nature of the coordinative binding of Cu(II) to Aβ, and provide insights that lead to a cure for AD.

The characterization of the fast kinetics of the Cu(II)–Aβ binding and interconversion between different species requires a tool with high structural and temporal resolution. Due to the sensitivity of molecular vibrations to their local chemical environments, Raman spectroscopy is a useful probe to study local structures.[18] Resonance Raman (RR) spectroscopy selectively

[a] *State Key Laboratory of Heavy Oil Processing, Center for Bioengineering & Biotechnology, China University of Petroleum (East China), Qingdao, 266580, P. R. China. E-mail: fhuang@upc.edu.cn*
[b] *Department of Chemistry, University of California, Irvine, CA 92698, USA. E-mail: yuz10@uci.edu*
[c] *Department of Chemistry, College of Science, China University of Petroleum (East China), Qingdao, 266580, P. R. China*
[d] *State Key Laboratory of Crystal Materials, Shandong University, Jinan, 250100, P. R. China*

† Electronic supplementary information (ESI) available. See DOI: 10.1039/c7cp06206k

‡ Current address: Pulse Institute, SLAC National Accelerator Laboratory, Menlo Park, CA 94025, USA.

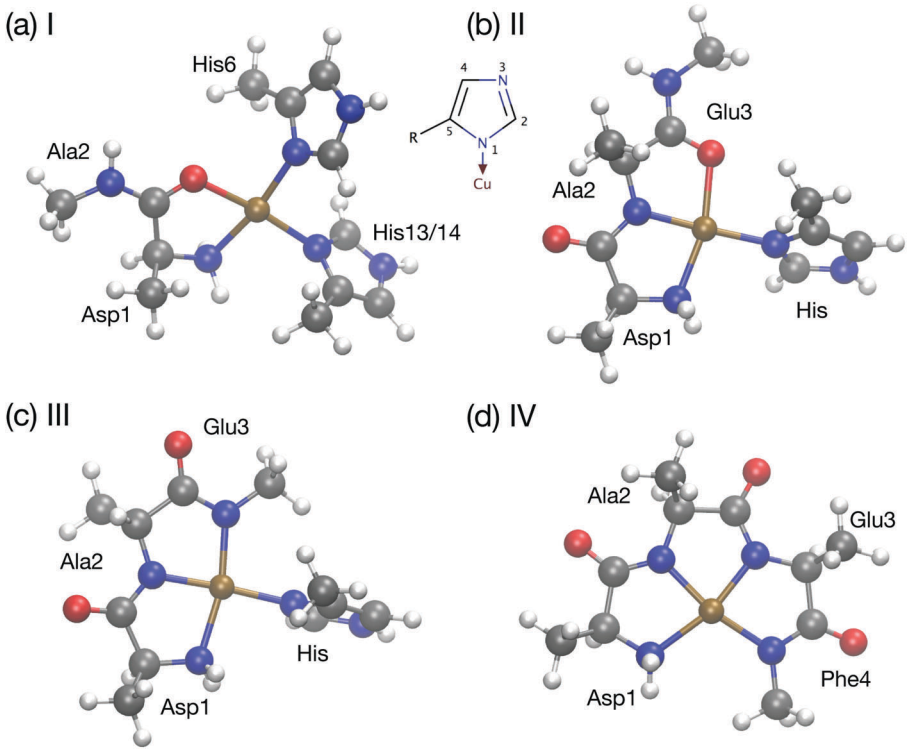

Fig. 1 (a)–(d) Structures of the Cu(II)–Aβ complexes I–IV, respectively. Residues from which nitrogen or oxygen atoms bonded to the central copper ion are labelled by their names. The residues are present in ascending order counterclockwise around the copper ion. Ochre, gray, blue, red and white balls represent copper, carbon, nitrogen, oxygen, and hydrogen atoms, respectively. The inset depicts the atomic labeling in the His imidazole ring.

enhances vibrational signatures strongly coupled with the selected electronic transitions of the chromophore.[19–24] Vibrational modes from water, peptides, or other environmental species can be filtered out by selecting the appropriate electronic excitations, making RR suitable for biological systems *in vivo* or *in vitro*. It has been shown that peptide or side-chain vibrations can be selectively enhanced by tuning the excitation resonant with the corresponding electronic transitions, enabling the characterization of protein secondary structures.[21,24–26] The Cu(II)–Aβ complexes exhibit absorption bands in the range above 300 nm, which is far away from the deep UV peptide π–π* bands at 190–210 nm and the aromatic side-chain bands around 230–280 nm.[21,25] These absorption bands in the near UV and visible range are ascribed to the d–d transitions of the Cu(II) ions and ligand-to-metal charge transfer (LMCT) transitions.[17] The separation of these bands from the peptide/side-chain bands provides the excitation selectivity required by RR detection. Furthermore, the electronic transitions of the Cu(II)–Aβ complexes are localized in the neighborhood of the metal ions, implying that only vibration modes involving metal ions or ligands would be active in the Raman process. These features enable RR to characterize the vibrational fingerprints of the complexes in a peptide abundant environment.

Ultrafast broad-band pulses have been widely used to investigate the dynamics of intra- or inter-molecular vibrational correlations in nonlinear spectroscopy experiments.[27–31] Ultrafast stimulated Raman measurement has been proposed by using a pump–probe configuration with off-resonant UV pulses[32] and resonant X-ray pulses.[33] However, extending RR to the valence excitation resonant region is not straightforward. In a multi-pulse experiment, pulses resonant to low lying valence excitations usually induce considerable excited state populations, due to the long lifetimes (ns) compared with pulse duration (~100 fs). Recently, we demonstrated that it is possible to enhance the resonance but not induce an excited state population by using pre-resonance pump pulses followed by a resonant probe pulse.[34] The signals can be collected at low sample concentrations due to the resonance enhancement. Moreover, the ultrafast temporal resolution enables the detection of transient structures during the binding or the interconversion processes.

In this paper, we report *ab initio* simulations on the spontaneous resonance Raman (spRR) and stimulated resonance Raman (stRR) spectra of the Cu(II)–Aβ complexes, and illustrated that these signals contain detailed structural information of the coordinative complexes. The spectral features are distinctive and can be directly related to the vibronic excitations of each complex, making it possible to capture both the spatial and temporal information simultaneously.

II. Theoretical protocols

We used a linearly displaced two-state harmonic nuclear Hamiltonian (Fig. 2) for the spectroscopic calculations (see the ESI† for details), where the dimensionless displacement between the potential energy minima of the excited state $|e\rangle$ and the ground state $|g\rangle$ was calculated using the excited state

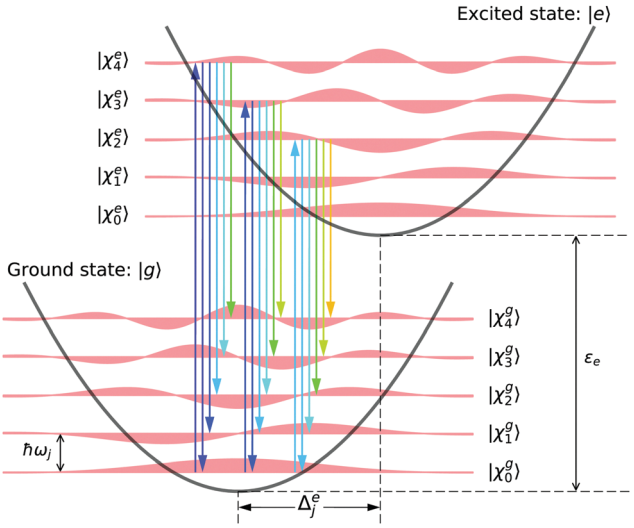

Fig. 2 Schematic view of the linearly displaced harmonic model describing the RR process. The potential energy surfaces of the ground (|g⟩) and excited (|e⟩) states are assumed to be harmonic near their equilibrium configurations with the same gradient. The difference between equilibrium configurations is denoted by a dimensionless reaction coordinate Δ_j corresponding to the j-th vibration mode with frequency ω_j.

gradient method.[26,34] The UV-vis absorption spectra were calculated using the cumulant expression.[35]

The Raman intensity is described by the differential Raman scattering cross section,[36]

$$\frac{\mathrm{d}\sigma}{\mathrm{d}\Omega} = \frac{I_{\mathrm{fi}}}{I_0} = \frac{\pi^2}{\varepsilon_0^2}\tilde{\nu}_0\tilde{\nu}_{\mathrm{fi}}^3|\alpha_{\mathrm{fi}}|^2 f_{\mathrm{i}}(T) \quad (1)$$

where I_0 and I_{fi} are the incident and outgoing light intensities, respectively. ε_0 is the vacuum permittivity, $\tilde{\nu}_0$ is the incident frequency (in wavenumber) and $\tilde{\nu}_{\mathrm{fi}}$ is the scattered wavenumber corresponding to a scattering process with the initial state i and the final state f. $f_{\mathrm{i}}(T)$ is the occupation probability of state i at temperature T, and α_{fi} is the transition polarizability. At resonance, the transition polarizability is given by

$$\alpha_{\mathrm{fi}} = \frac{1}{\hbar}(\mu_{\mathrm{eg}})^2 \sum_{\nu^{\mathrm{r}}\in|r\rangle} \frac{\langle\nu^{\mathrm{f}}|\nu^{\mathrm{r}}\rangle\langle\nu^{\mathrm{r}}|\nu^{\mathrm{i}}\rangle}{\omega_{\mathrm{e}} + \omega_{\nu^{\mathrm{r}}\nu^{\mathrm{i}}} - \omega_1 - \mathrm{i}\Gamma_{\mathrm{r}}}. \quad (2)$$

Here $|\nu^{\mathrm{i}}\rangle$, $|\nu^{\mathrm{f}}\rangle$ and $|\nu^{\mathrm{r}}\rangle$ are the initial, final and intermediate vibrational states, respectively. μ_{eg} is the electronic transition dipole moment; $\hbar\omega_1$, $\hbar\omega_{\mathrm{eg}}$, and $\hbar\omega_{\nu^{\mathrm{r}}\nu^{\mathrm{i}}}$ are the energy of the incident photon, the 0–0 electronic transition energy, and the vibrational part of the transition energy, respectively. In this work, we only consider the first order Franck–Condon (FC) contribution to the RR signals. Higher order Herzberg–Teller terms are neglected due to the fact that excitations are electronically strongly allowed.[37–39] This treatment is also referred to as the Albrech's "A term" approximation.[40]

The one-dimensional stimulated resonance Raman (1D stRR) signals can be measured in a two-pulse pump–probe experiment, where the pump pulse prepares a vibrational excited-state wavepacket in the ground electronic state *via* a pre-resonance Raman process, and the probe pulse arrives at the sample after a time delay to probe this wavepacket with a resonance Raman process. The signals are collected in the time domain as a function of the time delay τ, and the frequency domain signals can be obtained by a Fourier transform (see the ESI† for details),

$$S(\Omega_1) = \sum_{ac} P(a) \frac{\mathrm{i}\alpha_{ca}^{(1)}\left[\alpha_{ac}^{(2)} - \left(\alpha_{ac}^{(2)}\right)^*\right]}{\Omega_1 - \omega_{ca} + i\Gamma}, \quad (3)$$

where $\alpha_{ac}^{(i)}$ is the effective transition polarizability between the vibrational states a and c due to the i-th pulse,

$$\alpha_{ac}^{(i)} = \frac{1}{\pi}\sum_b \langle a|b\rangle\langle b|c\rangle|\mu_{\mathrm{eg}}|^2 \int_{-\infty}^{+\infty}\mathrm{d}\omega \frac{E_i^*(\omega)E_i(\omega+\omega_{ac})}{\omega+\omega_i-\omega_{bc}+i\Gamma_b} \quad (4)$$

Here $E_i(\omega)$ and ω_i are the spectral envelope and the center frequency of the i-th pulse. A detailed derivation of eqn (3) and (4) can be found in ref. 34. In the time domain calculations, we used Gaussian pulse envelopes with a full width at half maximum (FWHM) of 1768 cm^{-1} (8.33 fs) and a vibrational linewidth Γ = 10 cm^{-1}. The center frequencies of the pump pulses are chosen to be δ = 1500 cm^{-1}, below those of the corresponding probe pulses.[41] We adopted an all-parallel polarization configuration for the pump and probe pulses in the time domain simulation.

III. Computational models

Four proposed Cu(II)–Aβ complexes,[17] including the two forms present under physiological conditions, as well as the two forms existing in higher pH environments are studied. These proposed coordination structures agree well with recent kinetics studies[15,42] and binding site imaging.[11] However, there has been no direct evidence for the existence of these binding complexes so far. Our aim is to establish a correlation between different coordination structures and RR signatures, and illustrate the capability of RR to characterize various Cu(II)–Aβ complexes by probing their excitation-dependent vibronic effects. The structures are depicted in Fig. 1, where only the residues directly bound to Cu(II) are taken into account. To construct the computation models, we only break carbon–carbon bonds, with the broken bonds saturated by methyl groups.

As shown in Fig. 1, all four complexes have a tetracoordinated Cu(II) binding to carbonyl oxygen atoms, amino nitrogen atoms, or imidazole N1 atoms in His, with near planar coordination configurations. These complexes can be converted to each other by successive protonation (deprotonation) by decreasing (increasing) the pH. Specifically, in complex I, the Cu(II) ion binds to the terminal $-NH_2$, the –C═O from Asp1–Ala2, and two imidazole N1 atoms of His6 and His13/14; in complex II, the Cu(II) ion binds to the terminal $-NH_2$, the peptide N of Asp1–Ala2, the –C═O of Glu3, and one imidazole N1 atom; in complex III, the Cu(II) ion binds to the terminal $-NH_2$, the peptide N of Asp1–Ala2 and Ala2–Glu3, and the imidazole N1 of a His; in complex IV, the Cu(II) ion binds to the terminal $-NH_2$ and the three peptide N atoms of Asp1–Ala2, Ala2–Glu3, and Glu3–Phe4.

All the structures were fully optimized before spectroscopic calculations. The electronic structures were described at the level of density functional theory (DFT) with the PBE0 functional[43–45]

and the 6-311++G(d,p) basis set[46] implemented in the Gaussian 09 package.[47] The polarizable continuum model with conductor-like solvations (CPCM)[48,49] was used to simulate the aqueous environment. Time-dependent density functional theory (TD-DFT) was used to describe the electronic transitions and excited state properties. We performed natural transition orbital (NTO) analysis for the electronic transitions by extending the standard NTO protocol[50] to the open shell case, where the transition density matrices for the α and β spins were transformed separately by singular value decomposition. The energy gradients of the ground and excited states were both calculated analytically using Gaussian 09. All the vibrational frequencies were scaled by 0.97 to correct the systematic error in DFT frequency calculations.[51]

IV. Results and discussion

According to the proposed binding sites of Cu(II)–Aβ in different pH environments,[17] all four complexes studied here are open-shell structures, with net charges of +2, +1, 0, and −1, respectively. We first optimized the geometric structures of these complexes in their doublet and quadruplet states. The energy differences between different spin states are quite large (~3 eV, see Table S1, ESI†), which implicates that the contribution from higher spin states is negligible under moderate conditions. In the following, we will concentrate on the low-spin doublet spectroscopic properties of the four complexes.

A. Electronic structures and absorption spectra

We first examined the electronic transitions of the complexes to choose appropriate excitation wavelengths for the RR characterization. Since our aim is to characterize these complexes in a peptide abundant environment, avoiding the peptide absorption bands is a prerequisite for better visibility. There are two strong absorption bands in the peptide UV spectra; the one in the deep UV region (190–210 nm) originates from the peptide π–π* excitation, and another broader but weaker peak in the region of 220–280 nm is ascribed to the low-lying aromatic excitations from Tyr, Trp, or Phe residues. To utilize the excitation selectivity of the RR technique, we will concentrate on the RR bands corresponding to electronic excitations with wavelengths longer than 300 nm. The electronic transitions in this region can be classified into two categories: the lower energy bands around 600 nm originated from the copper ion d–d transitions, and the higher energy bands around 300 nm ascribed to the ligand-to-metal charge transfer (LMCT) excitations, where imidazole, amide, or amine ligands are involved.

All the considered excitations must be spin allowed, so that only transitions between orbitals contribute significantly to the excitations. For clarity, we denote the *i*-th electronic transition of complex S as ε_i^S. The spatial distributions of the NTOs are depicted in Fig. S2–S5 in the ESI;† it is interesting to note that all the transitions terminate in the β-LUMOs (*i.e.* the electron state) with Cu–ligand anti-bonding character for all the complexes.

The vibrationally resolved UV absorption spectra of complex I are depicted in Fig. 3(a). Five excitations contribute significantly

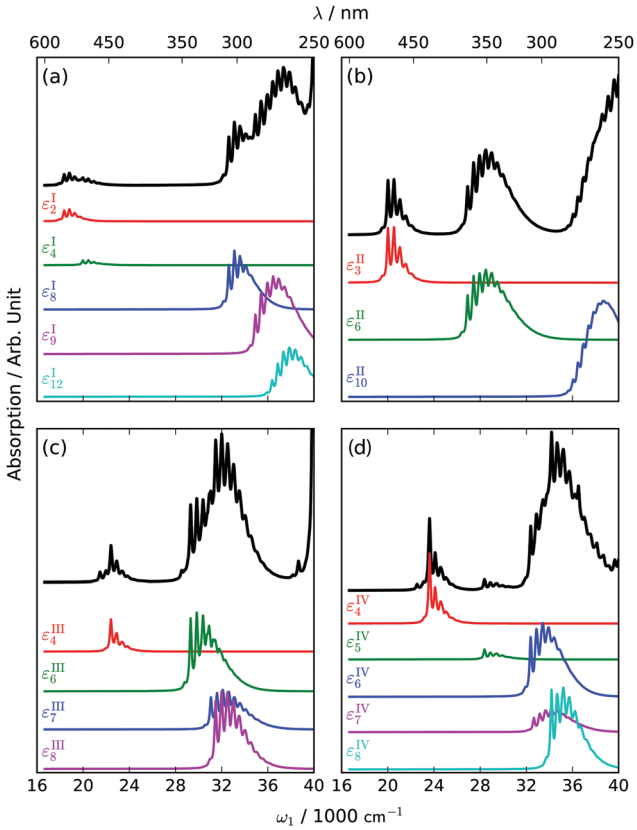

Fig. 3 (a)–(d) Vibration resolved UV-vis absorption spectra for complexes I–IV, respectively. The total absorption spectra are plotted in black. Electronic excitation resolved spectra with significant contributions are also provided, labeled by ε_i^S, which denotes the *i*-th electronic transition in system S.

to the total UV-vis spectrum. The weak d–d transitions at 545 (ε_2^I) and 500 (ε_4^I) nm are slightly blue-shifted compared with the experimental CD spectra,[17,52] since the adopted approximation ignores the protein environment. As shown in Fig. S1 (ESI†), ε_2^I is a typical d–d transition with the hole state localized at the metal center. However, in the hole state of ε_4^I, there is a considerable distribution on the imidazole ligand of His6, exhibiting bonding character, indicating an imidazole-to-Cu(II) LMCT component. ε_8^I at 306 nm is an imidazole LMCT transition with the hole state mainly composed of π bonding orbitals at the imidazole ligands from His6 and His13/14. The hole state of ε_9^I at 286 nm represents a lone pair at the amide oxygen, which is ascribed to an amide LMCT transition. ε_{12}^I at 275 nm contains an LMCT component both from the Asp1/Ala2 amide and the two imidazole ligands. Complex II was proposed to exist at pH 7.8–9.3.[3,17] The lowest excitation which has a considerable contribution to the UV spectrum is ε_3^{II} at 500 nm with a d–d transition character. The blue shift compared to that of complex I agrees well with the trends in previous spectroscopic measurements.[17] ε_6^{II} is an LMCT excitation with mixed imidazole and amide nitrogen to Cu(II) character at 372 nm. Another strong peak at 277 nm is ascribed to ε_{10}^{II}, which is an amide oxygen to Cu(II) LMCT transition.

Complex III was proposed to exist in the pH range of 9.3–10.2, and complex IV might appear as the pH value is even

higher. Although these two complexes might not exist under physiological conditions, accessing their spectroscopic signatures would facilitate the investigation of Cu(II)–peptide coordination. Four excitations contribute significantly to the complex III UV-vis spectrum: ε_4^{III} at 446 nm is a d–d transition; ε_6^{III} at 341 nm has a strong LMCT character from the amine and the Glu3 carbonyl lone-pair to the Cu(II) center; ε_7^{III} at 322 nm is similar to ε_6^{III}, but with LMCT from the Ala2 carbonyl lone-pair; ε_8^{III} at 318 nm is also an LMCT excitation from the amine and both the Ala2 and Glu3 carbonyl lone-pairs. The imidazole to Cu(II) LMCT is beyond the energy range we consider here. The latter three near degenerate excitations can be viewed as LMCTs from the Asp1, Ala2, and Glu3 to the metal ion. As shown in Fig. 1(d), complex IV is different from the other complexes, where the Cu(II) ion binds to the nitrogen atom in each of the first four residues but not in any His imidazole. The Cu(II) coordination also possesses a near planar configuration with Cu–N distances of 2.074, 1.934, 1.926, and 1.958 Å, respectively. The d–d transition ε_4^{IV} results in the lowest peak at 423 nm; the peaks around 352, 309, 306, and 293 nm can be ascribed to amide LMCT transitions.

Although UV-vis absorption itself cannot be used to identify the Cu(II)–Aβ complexes, it provides the possibility of characterizing these species by using RR with appropriate excitation wavelengths. This is a consequence of the fact that each complex has its own distinct electronic excitations beyond the peptide UV bands, ensuring a high signal-to-noise ratio (SNR) by filtering peptide Raman bands out.

B. Spontaneous Raman characteristics

The calculated two-dimensional spontaneous Raman (spRR) spectra of the Cu(II)–Aβ complexes are shown in Fig. 4. The 2D spRR signals are plotted with respect to the excitation frequency (ω_1, vertical axis) and the Raman shift (horizontal axis). The horizontal slices in Fig. 4 are the (pre-)resonance Raman spectra with the corresponding excitation energies, while the vertical slices represent the Raman excitation profiles for each specified vibration mode. There are also peaks along the direction tilted to the top right. These features are ascribed to the 0–1 vibronic excitations of the active modes.

The 2D spRR patterns in Fig. 4 of the four complexes exhibit distinct features both in the resonance excitation energies and

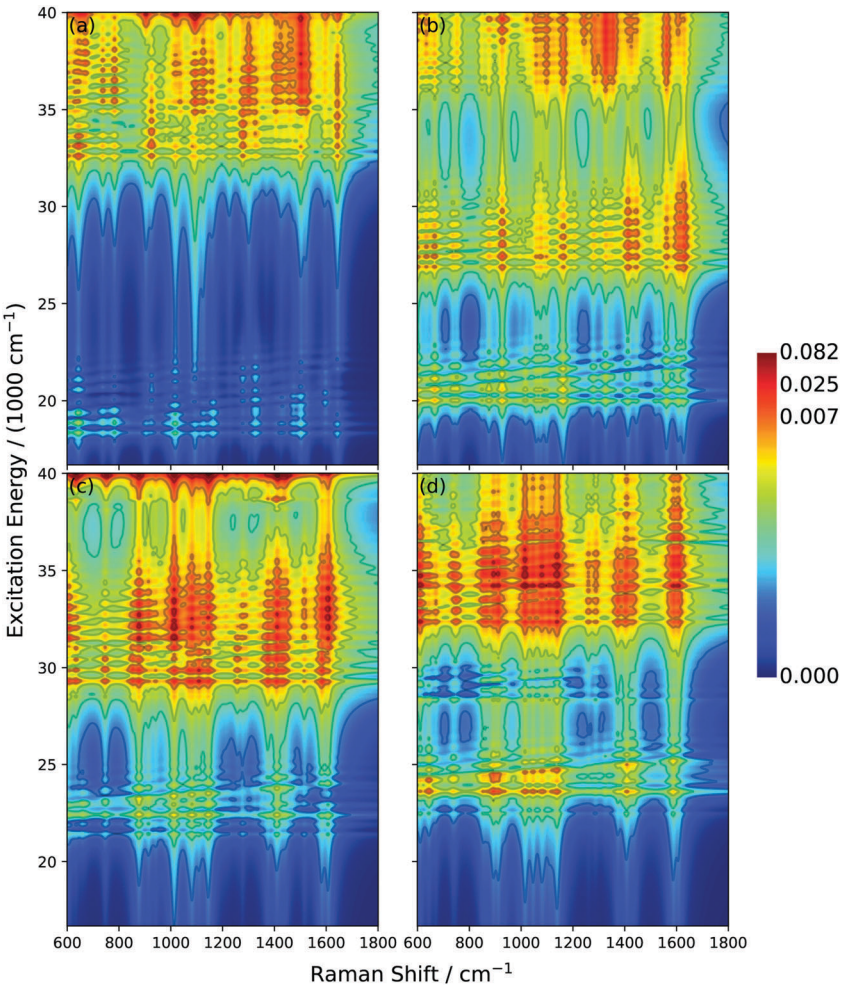

Fig. 4 (a)–(d) 2D spRR spectra of complexes I–IV. The horizontal and vertical axes represent the Raman shift and excitation energy, respectively. The spectra are displayed using the inverse hyperbolic sine function, which better reveals both weak and strong features,[34] $\bar{S}$ = arcsinh(CS), where a normalization coefficient C is chosen to make $\bar{S}$ close to 1.

the Raman active vibration modes. In the Franck–Condon regime, the transition polarizability can be viewed as the squared electronic transition dipole convoluted by a series of vibrational transitions; and a Raman excitation profile can be viewed as an absorption decorated by vibrational progressions. The relative Raman intensities with different excitation energies strongly depend on those of the corresponding electronic transitions. In Fig. 4(a), the Raman bands corresponding to d–d transitions at 545 nm ($\sim$18 400 cm^{-1}) and 500 nm ($\sim$20 000 cm^{-1}) are relatively weaker than those corresponding to the LMCT transitions in the region of 306–275 nm (32 600–36 400 cm^{-1}). The relative intensities are also shown in Fig. 5(a), where the horizontal slices with excitation frequencies coinciding with specific electronic transition energies are plotted. The RR spectra of $\varepsilon_2^{\mathrm{I}}$ and $\varepsilon_4^{\mathrm{I}}$ have been scaled 100 and 300 times, respectively, to be comparable to those of the LMCT transitions. Considering that the resonance enhancement of Raman intensities is about 10^6, and these two excitations are far separated from the LMCT and the peptide bands, these features might be highly detectable even at low concentrations.

As a result of the d–d transition dominated character of $\varepsilon_2^{\mathrm{I}}$, all the significant RR features are Cu-involving vibrations [Fig. 5(a)]: the Cu–imidazole stretching mode at 1016/1009 cm^{-1}, the Cu–Asp1 in-plane ring twisting at 782 cm^{-1}, and the Cu–Asp1 out-of-plane ring twisting at 737 cm^{-1}. The peptide AmI band only in the range of 1600–1700 cm^{-1} has much weaker features since $\varepsilon_2^{\mathrm{I}}$ has few peptide components. On the other hand, $\varepsilon_4^{\mathrm{I}}$ is a mixture of the d–d transition and the LMCT from the imidazole of His6. As a consequence, apart from the Cu–ligand stretching and twisting modes, the in-plane ring twisting of the corresponding imidazole at 1324 cm^{-1} is the strongest feature in the RR spectrum. $\varepsilon_8^{\mathrm{I}}$ is dominated by the LMCT transitions from both the imidazoles of His6 and His13/14; the most distinct features in its RR spectrum can be ascribed to a series of near-degenerate vibrational modes of the two imidazoles: the imidazole ring breath modes at 1277/1274 cm^{-1}, and the imidazole in-plane twisting modes at 925/924 cm^{-1}. As shown in Fig. S2 (ESI†), the hole state also has a considerable distribution along the Cu(II)–O(Asp1) bond, which leads to a pronounced Asp AmI peak at 1641 cm^{-1}. Both $\varepsilon_9^{\mathrm{I}}$ and $\varepsilon_{12}^{\mathrm{I}}$ are LMCT transitions mainly from Asp1, whereas the latter has slightly more contributions from the two imidazole rings. The spectra corresponding to these two excitations are dominated by peptide bands: the Asp1 AmI band at 1641 cm^{-1}, the Asp1 C_α–C_β stretching mode at 1500 cm^{-1}, the Asp1 C_α–H bending modes around 1300 cm^{-1}, and the Asp1 C–N stretching modes at 1157/1124 cm^{-1}. These distinctive spectroscopic features with different excitation energies demonstrate that the excitation selectivity of the RR technique can be ideally applied to the characterization of complex I, where vibrational signatures of the Cu–ligand bonds, the Asp1 peptide bonds, and the imidazole rings of His6 and/or His13/14 can be well resolved. Furthermore, the existence of the two imidazole rings brings near-degenerate signatures, which might be used to characterize the case of Cu(II) coordinated by the two His imidazoles.

Fig. 4(b) depicts the 2D spRR of complex II, and Fig. 5(b) depicts the horizontal slices (*i.e.* the spRR spectra) which

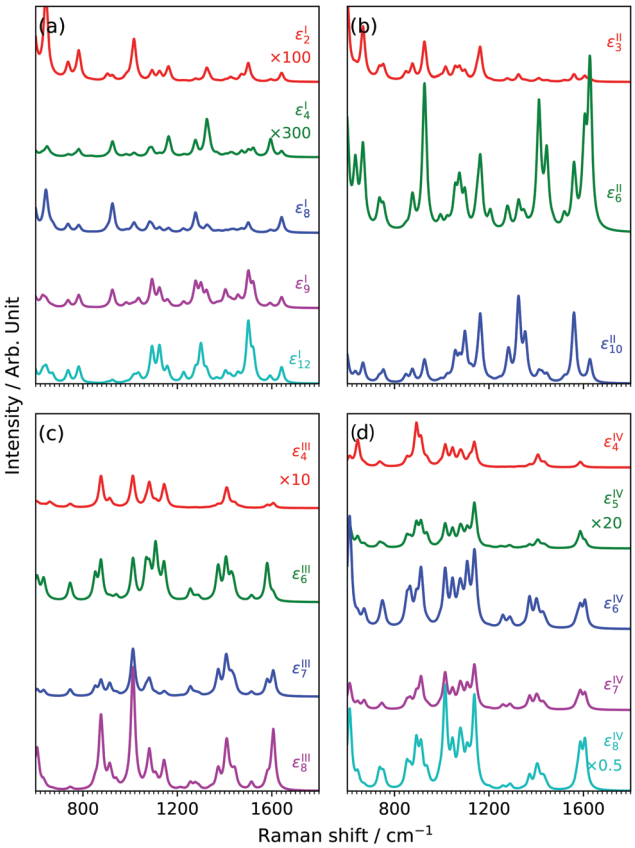

Fig. 5 (a)–(d) spRR spectra of complexes I–IV. Excitation energies are selected to be resonant to those of strong electronic transitions labeled by $\varepsilon_i^{\mathrm{S}}$.

correspond to $\varepsilon_3^{\mathrm{II}}$, $\varepsilon_6^{\mathrm{II}}$, and $\varepsilon_{10}^{\mathrm{II}}$, respectively. The $\varepsilon_3^{\mathrm{II}}$ excitation is dominated by the Cu(II) d–d transition mixed with a small portion of LMCT from the peptide bonds among Asp1, Ala2, and Glu3, and the His imidazole. The Cu–ligand modes only exhibit weak spRR signals, such as the Cu-Asp1 ring in-plane (out-of-plane) twisting at 875 (752) cm^{-1} and the Cu-Ala2 ring in-plane (out-of-plane) twisting at 847 (737) cm^{-1}. The most distinctive features are related to the peptide or the His imidazole modes, such as the peptide C–H bending coupled with the imidazole C2–H/N3–H bending modes at 1163 and 1162 cm^{-1}, and the imidazole in-plane twisting mode at 928 cm^{-1}. $\varepsilon_6^{\mathrm{II}}$ is a typical LMCT transition from both peptide and imidazole, hence the spRR spectra reveal features from both species. The three residues form two peptide bonds resulting in the near doubly degenerate AmI bands at 1627 and 1605 cm^{-1}. However, the AmII bands at 1559 and 1444 cm^{-1} are split due to the different chemical environments the nitrogen atoms reside in. The Raman peaks at 1411, 1346 and 1325 cm^{-1} are attributed to the AmIII bands of Ala2, Asp1, and Glu3, respectively. Another strong feature of the $\varepsilon_6^{\mathrm{II}}$ RR spectra is the imidazole ring twisting at 928 cm^{-1}. $\varepsilon_{10}^{\mathrm{II}}$ is an amide LMCT transition, with more contribution from the Cu-Ala2–Glu3 ring. As a consequence, the RR spectrum is dominated by the Ala2 and Glu3 peptide bands. The characteristic features are the Ala2 AmII band at 1559 cm^{-1}, the Ala2/Asp1 C_α–H bending band at 1325 cm^{-1}, and the Ala2 C–H bending band at 1163/1162 cm^{-1}.

Due to the absence of imidazole contribution in the ε_{10}^{II} hole state, the His imidazole modes are inactive in the corresponding spRR spectrum.

The 2D spRR spectra and their horizontal slices excited with specified electronic transition energies are shown in Fig. 4(c) and 5(c), respectively. Again, ε_4^{III}, the spRR spectra corresponding to the lowest d–d transition are relatively weak. In Fig. 5(c), the spRR spectrum of ε_4^{III} is scaled by 10 for better visibility. Similar to the case in complex I, this electronic excitation lies far away from other absorption bands, making its spRR spectrum useful for characterization. The hole state in Fig. S3 (ESI†) shows that apart from Cu(II) orbitals, there is a considerable contribution from the peptide bonds formed by Asp1, Ala2 and Glu3. These contributions can be illustrated from the ε_4^{III} spRR spectrum with the following features: the Cu–N(Glu3) bending coupled with Glu3 C–N stretching at 1406 cm^{-1}, the Cu–N(Ala2) stretching coupled with Ala2 C–N stretching at 1143 cm^{-1}, the Cu–Asp1–Ala2 ring twisting coupled with Asp1 C–H/N–H bending at 1082 cm^{-1}, Cu–Asp1–Ala2 ring twisting coupled with Ala2 C–H/N–H bending at 1011 cm^{-1}, and the Cu–Asp1–Ala2–Glu3 ring breath at 876 cm^{-1}. The other three electronic excitations considered here are LMCT transitions from Asp1, Ala2 and Glu3; hence the corresponding spRR spectra share similar features arising from peptide or Cu–peptide bonds. The NTOs in Fig. S3 (ESI†) show that the hole state of ε_6^{III} has a considerable contribution from the Ala2 carbonyl lone pair, whereas for ε_7^{III} and ε_8^{III} the Asp carbonyl lone pair contributes significantly. This can be directly seen from the spRR spectra in Fig. 5(c): in the spRR spectrum excited by ε_6^{III}, the Ala2 AmI peak at 1580 cm^{-1} dominates the AmI bands, while the Asp AmI peak at 1606 cm^{-1} is much stronger than the Ala2 AmI peak for the ε_7^{III} and ε_8^{III} excited spectra.

The Cu(II) ion binds to the first four residues in complex IV and forms three five-membered rings. This is the only complex that does not contain imidazole from His in this study. In all three five-membered rings, Cu(II) binds to the peptide N atoms and the carbonyl groups point to the outside. This structural similarity leads to triply or quadruply near degenerate peptide features of the vibration modes observed in the RR spectra. For instance, the three peaks at 1606, 1586, and 1572 cm^{-1} are attributed to the AmI mode of Asp1, Ala2, and Glu3, respectively. The other Raman active peptide bands are rather complex because several atoms are involved and the mode itself is composed of stretching, bending, or twisting motions. As shown in Fig. 5(d), the spRR bands around 1370–1410 cm^{-1} arise from a series of modes with coupled peptide C–H bending and C–N stretching from the four amide ligands; while the bands in the range of 1010–1140 cm^{-1} can be ascribed to the C–N stretching coupled with the C–H bending modes in the peptides. These two bands are similar to the AmII ($\sim$1550 cm^{-1}) and AmIII (1200–1340 cm^{-1}) bands of free peptides. The blue shifted vibrational energy is a result of the confined configuration caused by Cu(II) coordination. The five-membered ring twisting modes are also characteristic of complex IV, with the in-plane modes at 892, 866, and 852 cm^{-1}, and the out-of-plane modes at 754, 746, and 736 cm^{-1}.

C. One-dimensional stimulated resonance Raman signals

The 1D stRR signals of the four complexes are shown in Fig. 6. In the 1D stRR experiment, the pump pulse is chosen to be preresonant with a specified electronic excitation to avoid high excited state occupation before the arrival of the probe pulse. The parallel pulse configurations used in the calculation are denoted by the pulse center frequencies ($\varepsilon - \delta$, ε), where δ = 1500 cm^{-1}. Considering that the pump should not be (near-)resonant with any electronic transitions of the system, the frequency combinations of the pump and probe pulses are restricted. Only two pulse configurations for each complex were considered in the calculation, which generate two stRR signals.

As shown in Fig. 6, similar to the spRR signals (dashed lines), the stRR signals (solid lines) of the four complexes have distinctive features, ensuring their capability for structure characterization. Although the 1D stRR spectra resemble the main features of their spRR counterparts, the relative intensities of the peaks vary. A strong signal in the stRR spectra implies that the corresponding vibrational excitation survives the time delay between the pump and probe pulses and hence produces a strong correlation. Furthermore, the survived signals were enhanced twice by the two pulses, resulting in a much higher visibility. For instance, Fig. 6(a) depicts the stRR signals with the pulse configuration ($\varepsilon_2^I - \delta$, ε_2^I) and the spRR signals excited

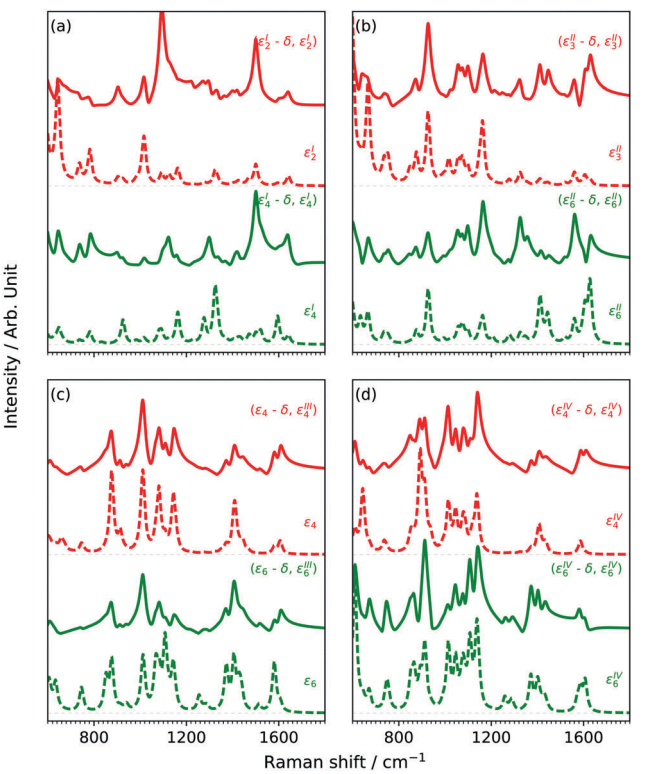

Fig. 6 (a)–(d) Comparison between stRR (solid) and spRR (dashed) spectra of complexes I–IV, respectively. The center frequencies of the pump and probe pulses used in the stRR simulation are denoted as ($\varepsilon - \delta$, ε), with the pump chosen to be pre-resonant and resonant with a specified electronic transition. The frequency difference between the pump and probe pulses δ = 1500 cm^{-1} in the simulations.

with ε_2^I. The relative intensities of the active modes are different: the peaks at 1091 and 1227 cm^{-1} pronounced in the stRR turn out to be relatively weak in the spRR spectrum. These two peaks are assigned to the Asp1 NH bending and Asp1 coupled NH–CH bending modes. We note that the electronic state of the ε_2^I transition has a considerable distribution on the Asp N–H bond, indicating strong vibronic coupling. The NH bending or coupled CH–NH bending modes in the other Cu(II)–amine binding complexes also survive in the pump–probe detection of other complexes as shown in Fig. 6. These features can be used to characterize the direct binding of Cu(II) to the amino N atoms (Tables 1–4).

In addition, the 1D stRR experiments could be conducted at the femto-second time scale, which is fast enough to capture the transient intermediates during the Cu(II)–Aβ binding. Combined with the higher SNR of the vibronic strongly coupled modes to the specified electronic transitions, stRR is a useful tool to characterize the local chemical environment and to identify microscopic structures in complex surroundings, even during nonequilibrium processes. The high spatial and temporal resolution and high SNR make this technique a powerful tool for dynamical characterization of biochemical reactions.

Table 1 Raman active modes of complex I. All frequencies are wavenumbers

Frequency/cm^{-1}	Description
1641	AmI of Asp1
1595	Imidazole C4–C5 stretching of His6
1593	Imidazole C4–C5 stretching of His13/14
1517	N1–C2–N3 bending of His6 and His13/14
1521	N1–C2–N3 bending of His6 and His13/14
1500	C_α–C_β stretching of Asp1
1456	NH bending of Asp1
1403	AmII of Asp 1
1323	Imidazole in-plane ring twisting of His13/14
1324	Imidazole in-plane ring twisting of His6
1274	Imidazole ring breathing of His6 and His13/14
1277	Imidazole ring breathing of His6 and His13/14
1124	C_α–N stretching of Asp1
1080	Imidazole CH and NH bending of His6
1081	Imidazole CH and NH bending of His13/14
1016	Cu–N1@imidazole stretching coupled with imidazole CH/NH bending
1009	Cu–N1@imidazole stretching coupled with imidazole CH/NH bending
925	Imidazole in-plane ring twisting of His6
924	Imidazole in-plane ring twisting of His13/14
782	Asp1-Cu ring in-plane twisting
737	Asp1-Cu ring out-of-plane twisting

Table 2 Raman active modes of complex II. All frequencies are wavenumbers

Frequency/cm^{-1}	Description
1627	AmI of Asp1
1605	AmI of Ala2
1559	AmII of Ala2
1444	AmII of Asp1
1411	AmIII of Ala2
1346	AmIII of Asp1
1325	AmIII of Glu3
1325	C_αH bending of Ala2 and Asp1
1279	CH bending of Asp1 and Ala2
1276	C_β–imidazole stretching of His
1163	CH bending of Ala2 with C2–H/N3–H bending of His imidazole
1162	CH bending of Ala2 with C2–H/N3–H bending of His imidazole
1097	NH bending and C_α–N stretching of Asp 1
1080	Imidazole C4–H bending of His
1097	C_αN stretching of Asp1
1056	C_βH bending of Ala2
928	Imidazole in-plane ring twisting of His
875	Asp1-Cu ring in-plane twisting
847	Ala2-Cu ring in-plane twisting
752	Asp1-Cu ring out-of-plane twisting
737	Ala2-Cu ring out-of-plane twisting

Table 3 Raman active modes of complex III. All frequencies are wavenumbers

Frequency/cm^{-1}	Description
1606	AmI of Asp1
1592	Imidazole C4–C5 stretching of His
1580	AmI of Ala2
1513	Imidazole C2–H bending with N1–C2 stretching
1466	Imidazole N3–H bending
1411	C_α–N stretching of Ala2
1406	CN stretching of Glu3/Cu–N(Glu3) bending
1326	Imidazole ring in-plane twisting
1290	C_α–H bending of Ala2
1276	C_β–imidazole stretching of His
1273	C_α–H bending of Asp1
1254	C_α–H bending with CC stretching of Ala2
1220	Imidazole CH and NH bending of His
1143	CN stretching of Ala2/Cu–N(Ala2) stretching
1108	CN stretching of Glu3
1082	CH and NH bending of Asp1
1078	Imidazole C4–H bending of His
1011	CH and NH bending of Asp1 and Ala2/Cu-Asp1–Ala2 ring in-plane twisting
926	Imidazole ring in-plane twisting
913	Cu–N stretching of Ala2
876	Asp1-Cu and Ala2-Cu ring breath
754	Asp1-Cu ring out-of-plane twisting
746	Ala2-Cu ring out-of-plane twisting

Table 4 Raman active modes of complex IV. All frequencies are wavenumbers

Frequency/cm^{-1}	Description
1606	AmI of Asp1
1586	AmI of Ala2
1572	AmI of Glu3
1410	CH bending coupled with CN stretching of Ala2 and Glu3
1407	CN stretching of Ala2 and Glu3
1400	CN stretching of Phe4
1372	CN stretching of Phe4
1290	CH bending of Ala2
1284	CH bending of Glu3
1277	CH bending of Asp1
1258	CH bending of Ala2 and Glu3
1248	CH bending of Ala2 and Glu3
1138	CN stretching and CH bending of Glu3
1107	CN stretching and CH bending of Phe4
1086	CN stretching and CH bending of Asp1
1046	CN stretching and CH bending of Ala2
1014	CH bending of Glu3
912	Cu–N stretching of Ala2
892, 866, 852	Cu-residue ring in-plane twisting
754, 746, 736	Cu-residue ring out-of-plane twisting

V. Conclusions

We simulated the vibrationally resolved UV-vis absorption, the spRR and the 1D stRR spectra using simple molecular models

of the Cu(II)–Aβ binding complexes. Complexes I and II are proposed to play an important role in the early stages of A aggregation, and the other two complexes are also helpful in the study of Cu(II)–Aβ binding. The detailed spectroscopic patterns and characteristics are discussed and their relation to the vibration modes in specific local chemical environments is revealed. We found distinct features in the spRR and stRR spectra for each complex, which are sufficient for the identification of these species. By virtue of the resonance enhancement, spRR and stRR are ideal tools for chemical characterization of the ultra low concentration samples in life science studies. Furthermore, the stRR technique has a time resolution of femtoseconds, which is sufficient to capture the dynamical details during metal–protein binding. Complementary to existing nuclear magnetic resonance (NMR) and electron paramagnetic resonance (EPR) measurements, together these techniques can be used to reveal the microscopic dynamical details of the Cu(II)–Aβ binding and induced aggregation.

Conflicts of interest

There are no conflicts to declare.

Acknowledgements

We acknowledge financial support from the National Natural Science Foundation of China (NSFC, Grant No. 21403300, 21573129, and 21773309), the China Postdoctoral Science Foundation (Grant No. 2014M560587). Part of the calculations was carried out at the National Supercomputing Center in Shanghai.

References

1 J. Nasica-Labouze, P. H. Nguyen, F. Sterpone, O. Berthoumieu, N.-V. Buchete, S. Coté, A. De Simone, A. J. Doig, P. Faller and A. Garcia, *et al.*, *Chem. Rev.*, 2015, **115**, 3518.
2 A. T. Petkova, Y. Ishii, J. J. Balbach, O. N. Antzutkin, R. D. Leapman, F. Delaglio and R. Tycko, *Proc. Natl. Acad. Sci. U. S. A.*, 2002, **99**, 16742.
3 C. Hureau and P. Dorlet, *Coord. Chem. Rev.*, 2012, **256**, 2175.
4 P. Faller, C. Hureau and G. La Penna, *Acc. Chem. Res.*, 2014, **47**, 2252.
5 A. Budimir, *Acta Pharm.*, 2011, **61**, 1.
6 T. Karelina, O. Demin Jr, O. Demin, S. Duvvuri and T. Nicholas, *CPT: Pharmacometrics Syst. Pharmacol.*, 2017, **924**, 17.
7 L. N. Zhao, H. W. Long, Y. Mu and L. Y. Chew, *Int. J. Mol. Sci.*, 2012, **13**, 7303.
8 W. F. Goure, G. A. Krafft, J. Jerecic and F. Hefti, *Alzheimer's Res. Ther.*, 2014, **6**, 42.
9 N. Malakooti, M. A. Pritchard, P. A. Adlard and D. I. Finkelstein, *Front. Aging Neurosci.*, 2014, **6**, 11007.
10 R. A. Himes, G. Y. Park, G. S. Siluvai, N. J. Blackburn and K. D. Karlin, *Angew. Chem., Int. Ed.*, 2008, **47**, 9084.
11 D. Yugay, D. P. Goronzy, L. M. Kawakami, S. A. Claridge, T.-B. Song, Z. Yan, Y.-H. Xie, J. Gilles, Y. Yang and P. S. Weiss, *Nano Lett.*, 2016, **16**, 6282.
12 F. Hane, G. Tran, S. J. Attwood and Z. Leonenko, *PLoS One*, 2013, **8**, e59005.
13 C. D. Syme, R. C. Nadal, S. E. J. Rigby and J. H. Viles, *J. Biol. Chem.*, 2004, **279**, 18169.
14 L. Hou and M. G. Zagorski, *J. Am. Chem. Soc.*, 2006, **128**, 9260.
15 T. Branch, P. Girvan, M. Barahona and L. Ying, *Angew. Chem., Int. Ed.*, 2014, **54**, 1227.
16 J. T. Pedersen, C. B. Borg, T. C. T. Michaels, T. P. J. Knowles, P. Faller, K. Teilum and L. Hemmingsen, *ChemBioChem*, 2015, **16**, 1293.
17 B. Alies, H. Eury, C. Bijani, L. Rechignat, P. Faller and C. Hureau, *Inorg. Chem.*, 2011, **50**, 11192.
18 D. A. Long, *The Raman Effect: A Unified Treatment of the Theory of Raman Scattering by Molecules*, John Wiley & Sons Ltd, Chichester, 1st edn, 2002.
19 S. A. Oladepo, K. Xiong, Z. Hong and S. A. Asher, *J. Phys. Chem. Lett.*, 2011, **2**, 334.
20 S. A. Oladepo, K. Xiong, Z. Hong, S. A. Asher, J. Handen and I. K. Lednev, *Chem. Rev.*, 2012, **112**, 2604.
21 J. Xiong and R. D. JiJi, *Biophys. Chem.*, 2017, **220**, 42.
22 M. Wang and R. D. JiJi, *Biophys. Chem.*, 2011, **158**, 96.
23 T. Miura, K. Suzuki and H. Takeuchi, *J. Mol. Struct.*, 2001, **598**, 79.
24 V. A. Shashilov, V. Sikirzhytski, L. A. Popova and I. K. Lednev, *Methods*, 2010, **52**, 23.
25 L. A. Popova, R. Kodali, R. Wetzel and I. K. Lednev, *J. Am. Chem. Soc.*, 2010, **132**, 6324.
26 H. Ren, J. Jiang and S. Mukamel, *J. Phys. Chem. B*, 2011, **115**, 13955.
27 M. Kubo, F. Gruia, A. Benabbas, A. Barabanschikov, W. Montfort, E. Maes and P. Champion, *J. Am. Chem. Soc.*, 2008, **130**, 9800.
28 P. Kukura, D. W. McCamant and R. A. Mathies, *Annu. Rev. Phys. Chem.*, 2007, **58**, 461.
29 S. D. Moran, A. M. Woys and L. E. Buchanan, *Proc. Natl. Acad. Sci. U. S. A.*, 2012, **109**, 3329.
30 H. Frostig, T. Bayer, N. Dudovich, Y. C. Eldar and Y. Silberberg, *Nat. Photonics*, 2015, **9**, 339.
31 A. P. Spencer, W. O. Hutson and E. Harel, *Nat. Commun.*, 2017, **8**, 1.
32 Y. Tanimura and S. Mukamel, *J. Chem. Phys.*, 1993, **99**, 9496.
33 J. D. Biggs, Y. Zhang, D. Healion and S. Mukamel, *J. Chem. Phys.*, 2012, **136**, 174117.
34 H. Ren, J. D. Biggs and S. Mukamel, *J. Raman Spectrosc.*, 2013, **44**, 544.
35 S. Mukamel, *Principles of Nonlinear Optical Spectroscopy*, Oxford University Press, New York, Oxford, 1995, 1st edn.
36 S. A. Asher, *Annu. Rev. Phys. Chem.*, 1988, **39**, 537.
37 H. Ma, J. Liu and W. Liang, *J. Chem. Theory Comput.*, 2012, **8**, 4474.
38 F. J. Avila Ferrer, V. Barone, C. Cappelli and F. Santoro, *J. Chem. Theory Comput.*, 2013, **9**, 3597.
39 Z. Y. Gong, G. Tian, S. Duan and Y. Luo, *J. Chem. Theory Comput.*, 2015, **11**, 5385.
40 A. C. Albrecht, *J. Chem. Phys.*, 1961, **34**, 1476.

41 H. Ren, Z. Lai, J. D. Biggs, J. Wang and S. Mukamel, *Phys. Chem. Chem. Phys.*, 2013, **15**, 19457.
42 L. G. Trujano-Ortiz, F. J. González and L. Quintanar, *Inorg. Chem.*, 2015, **54**, 4.
43 J. P. Perdew, K. Burke and M. Ernzerhof, *Phys. Rev. Lett.*, 1996, **77**, 3865.
44 J. P. Perdew, K. Burke and M. Ernzerhof, *Phys. Rev. Lett.*, 1997, **78**, 1396.
45 R. D. Amos, *Chem. Phys. Lett.*, 1982, **87**, 23.
46 M. J. Frisch, J. A. Pople and J. S. Binkley, *J. Chem. Phys.*, 1984, **80**, 3265.
47 M. J. Frisch, G. W. Trucks, H. B. Schlegel, G. E. Scuseria, M. A. Robb, J. R. Cheeseman, G. Scalmani, V. Barone, B. Mennucci and G. A. Petersson, *et al.*, *Gaussian09 Revision D.01*, Gaussian Inc., Wallingford CT, 2009.
48 V. Barone and M. Cossi, *J. Phys. Chem. A*, 1998, **102**, 1995.
49 M. Cossi, N. Rega, G. Scalmani and V. Barone, *J. Comput. Chem.*, 2003, **24**, 669.
50 R. L. Martin, *J. Chem. Phys.*, 2003, **118**, 4775.
51 J. P. Merrick, D. Moran and L. Radom, *J. Phys. Chem. A*, 2007, **111**, 11683.
52 J. Li and Y. Zhang, *Cryst. Res. Technol.*, 1991, **26**, 331.